

Behavior of Mn-Ni-Si rich precipitate in RPV steel: Linking CALPHAD to phase-field method

Kunok Chang, Gyeong-Geun Lee, Junhyun Kwon

Korea Atomic Energy Research Institute, Daejeon, Korea, 34057
kunokchang@kaeri.re.kr

Abstract - We performed phase-field modeling to evaluate the stability of Mn-Ni-Si (MNS) precipitates in a Fe-Mn-Ni-Si quaternary system. We adopted the UW1 quaternary database to perform the quantitative simulation. We examined the stability of T3, T6, and T7 precipitates. We found that the T6 precipitate is stable, while the other two are unstable; this observation is consistent with the results of thermodynamic modeling and experimental observations.

I. INTRODUCTION

Irradiation-enhanced precipitation hardening is known as one of the main sources of the late-stage embrittlement of reactor pressure vessel (RPV) steel [1, 2, 3, 4, 5]. Even in low-Cu steel, Mn-Ni-Si (MNS) precipitates can be present in the stable form [3, 4, 5], and the MNS phases in RPV steel have been investigated using experimental [4, 5] and computational[3] methods. Xiong et al. assessed the thermodynamic database for the Fe-Mn-Ni-Si quaternary system, i.e., the UW1 database, and the results were compared with the output of the commercialized database TCAL2 [3]. In this study, we adopt the phase-field method to describe both thermodynamic and kinetic features of the Fe-Mn-Ni-Si quaternary system. Cu-containing precipitates of the low alloy Fe have already been investigated using the phase-field method [6, 7, 8]. Koyama et al. assessed the thermodynamic database for the Fe-Cu-Mn-Ni quaternary system [6, 7], and the phase-field method was used to investigate the kinetic and elastic aspects of the Fe-Cu-Mn-Ni system. We extended the binary KKS model [9] to the quaternary system to perform the simulation for the Fe-Mn-Ni-Si system. We considered four phases (one matrix and three precipitate phases) in our simulation. We proposed the framework that enables us to predict the stability of the precipitates in RPV steel by considering both thermodynamics and kinetics. The UW1 thermodynamic database [3] was used to perform the simulations of the precipitate behavior in the bcc Fe matrix of the quaternary system. We compared the stability of various types of precipitates in a low-alloy steel. Further, our predicted precipitate stability was compared with the prediction results of thermodynamic modeling [3] and experimental observations [4, 5].

II. UW1 CALPHAD DATABASE

We adopted the UW1 CALPHAD database to simulate the microstructural evolution of the Fe-Mn-Ni-Si system [3]. One bcc phase for the matrix and 12 MNS precipitate phases are considered. In our study, we selected one bcc phase and three MNS precipitate phases for simplicity. The thermodynamic parameters we used were taken from the supplementary material of ref. [3] as follows:

For bcc (Fe,Mn,Ni,Si) phase,

$$\begin{aligned} {}^0L_{Fe,Mn}^{bcc} &= -2759 + 1.23T \\ {}^0L_{Fe,Ni}^{bcc} &= -956.63 - 1.28726T \\ {}^1L_{Fe,Ni}^{bcc} &= 1789.03 - 1.92912T \\ {}^0L_{Fe,Si}^{bcc} &= -153138.56 + 46.48T \\ {}^1L_{Fe,Si}^{bcc} &= -92352 \\ {}^2L_{Fe,Si}^{bcc} &= 62240 \\ {}^0L_{Mn,Ni}^{bcc} &= -3508.43 - 23.7885T \\ {}^0L_{Mn,Si}^{bcc} &= -89620.7 + 2.9410T \\ {}^1L_{Mn,Si}^{bcc} &= -7500.0 \\ {}^0TC_{Fe,Mn}^{bcc} &= 123 \\ {}^0TC_{Fe,Si}^{bcc} &= 504 \end{aligned}$$

For T3 : $Mn_{6/29}Ni_{16/20}Si_{7/20}$ phase,

$$\begin{aligned} {}^0G_{Mn,Ni,Si}^{T3} &= -48186.497 + 6/29^0G_{Mn}^{bcc} \\ &+ 16/29^0G_{Ni}^{fcc} + 7/29^0G_{Si}^{diamond} \end{aligned}$$

For T6 : $Mn_{1/3}(Ni, Si)_{2/3}$ phase,

$$\begin{aligned} {}^0G_{Mn,Ni}^{T6} &= 10086.99 + 1/3^0G_{Mn}^{bcc} + 2/3^0G_{Ni}^{fcc} \\ {}^0G_{Mn,Si}^{T6} &= 1666.67 + 1/3^0G_{Mn}^{bcc} + 2/3^0G_{Si}^{fcc} \\ {}^0L_{Mn,Ni,Si}^{bcc} &= -159474.81, {}^1L_{Mn,Ni,Si}^{bcc} = -172110.47 \end{aligned}$$

For T7 : $Mn_{1/2}Ni_{1/3}Si_{1/6}$ phase,

$$\begin{aligned} {}^0G_{Mn,Ni,Si}^{T7} &= -32434.25 - 5T + 1/2^0G_{Mn}^{bcc} \\ &+ 1/3^0G_{Ni}^{fcc} + 1/6^0G_{Si}^{diamond} \end{aligned}$$

III. PHASE-FIELD MODEL

We utilized the phase-field model to simulate the microstructural evolution of the Fe-Mn-Ni-Si system. We solved the Cahn-Hilliard [10] and Allen-Cahn (Ginzburg-Landau) equations [11] to simulate the microstructural evolution.

We will denote the composition ($i = 1, 2, 3, 4$ for Fe, Mn, Ni, Si, respectively) in the phase θ using $c_i^\theta(\mathbf{r}, t)$ at position

\mathbf{r} and time t . θ indicates the T3, T6, and T7 phases. We introduce four non-conserved order parameter (ϕ^i) to indicate the regions of the four precipitated phases. Composition $c_i(\mathbf{r}, t)$ is given as follows [9]:

$$c_i(\mathbf{r}, t) = c_i^{T3}(\mathbf{r}, t)h(\phi^{T3}) + c_i^{T6}(\mathbf{r}, t)h(\phi^{T6}) + c_i^{T7}(\mathbf{r}, t)h(\phi^{T7}) + c_i^\alpha(\mathbf{r}, t)[1 - \sum_\theta h(\phi^\theta)] \quad (1)$$

where[12],

$$h(\phi^\theta) = (\phi^\theta)^3[6(\phi^\theta)^2 - 15\phi^\theta + 10] \quad (2)$$

The local free energy density $G(c_i^\theta, t)$ of the system is expressed as follows:

$$G(c_i^\theta, t) = h(\phi^{T3})G^{T3} + h(\phi^{T6})G^{T6} + h(\phi^{T7})G^{T7} + [1 - \sum_\theta h(\phi^\theta)]G^\alpha(c_i^\alpha, t) + g(\phi^\theta) \quad (3)$$

where,

$$G^\alpha(c_i^\alpha, t) = c_1^\alpha \times^0 G_{Fe}^{bcc} + c_2^\alpha \times^0 G_{Mn}^{bcc} + c_3^\alpha \times^0 G_{Ni}^{bcc} + c_4^\alpha \times^0 G_{Si}^{bcc} + RT[c_1^\alpha \log(c_1^\alpha) + c_2^\alpha \log(c_2^\alpha) + c_3^\alpha \log(c_3^\alpha) + c_4^\alpha \log(c_4^\alpha)] + L_{Fe,Mn}^{bcc} c_1^\alpha c_2^\alpha + L_{Fe,Ni}^{bcc} c_1^\alpha c_3^\alpha + L_{Fe,Si}^{bcc} c_1^\alpha c_4^\alpha + L_{Mn,Ni}^{bcc} c_2^\alpha c_3^\alpha + L_{Mn,Si}^{bcc} c_2^\alpha c_4^\alpha \quad (4)$$

where $c_1^\alpha = 1.0 - c_2^\alpha - c_3^\alpha - c_4^\alpha$.

From ref.[13], we obtain the free energy of each element of the α phase.

The free energy of the T3, T6, and T7 precipitates is given as follows:

$$G^{T3} =^0 G_{Mn,Ni,Si}^{T3} \quad (5)$$

$$G^{T6}(c_i^{T6}, t) = y_3^{II} \times^0 G_{Mn,Ni}^{T6} + y_4^{II} \times^0 G_{Mn,Si}^{T6} + 2/3RT [y_3^{II} \log(y_3^{II}) + y_4^{II} \log(y_4^{II})] + y_3^{II} y_4^{II} L_{Mn:Ni,Si}^{bcc} \quad (6)$$

y_3^{II} and y_4^{II} denote the site fraction of Ni and Si at the second sub-lattice of the T6 phase, respectively.

$$G^{T7} =^0 G_{Mn,Ni,Si}^{T7} \quad (7)$$

1. Chemical potential and Diffusion potential

In the bcc (α phase), the chemical potentials of each species is given as follows:

$$\mu_1^\alpha(T, P, c_i^\alpha) =^0 G_{Fe}^{bcc} + RT \log(c_1^\alpha) + L_{Fe,Mn}^{bcc} c_2^\alpha (c_2^\alpha + c_3^\alpha + c_4^\alpha) + L_{Fe,Ni}^{bcc} c_3^\alpha (c_2^\alpha + c_3^\alpha + c_4^\alpha) + L_{Fe,Si}^{bcc} c_4^\alpha (c_2^\alpha + c_3^\alpha + c_4^\alpha) - L_{Mn,Ni}^{bcc} c_2^\alpha c_3^\alpha - L_{Mn,Si}^{bcc} c_2^\alpha c_4^\alpha \quad (8)$$

$$\mu_2^\alpha(T, P, c_i^\alpha) =^0 G_{Mn}^{bcc} + RT \log(c_2^\alpha) + L_{Fe,Mn}^{bcc} c_1^\alpha (c_1^\alpha + c_3^\alpha + c_4^\alpha) + L_{Mn,Ni}^{bcc} c_3^\alpha (c_1^\alpha + c_3^\alpha + c_4^\alpha) + L_{Mn,Si}^{bcc} c_4^\alpha (c_1^\alpha + c_3^\alpha + c_4^\alpha) - L_{Fe,Ni}^{bcc} c_1^\alpha c_3^\alpha - L_{Fe,Si}^{bcc} c_1^\alpha c_4^\alpha \quad (9)$$

$$\mu_3^\alpha(T, P, c_i^\alpha) =^0 G_{Ni}^{bcc} + RT \log(c_3^\alpha) - L_{Fe,Mn}^{bcc} c_1^\alpha c_2^\alpha + L_{Fe,Ni}^{bcc} c_1^\alpha (c_1^\alpha + c_2^\alpha + c_4^\alpha) + L_{Mn,Ni}^{bcc} c_2^\alpha (c_1^\alpha + c_2^\alpha + c_4^\alpha) - L_{Fe,Si}^{bcc} c_1^\alpha c_4^\alpha - L_{Mn,Si}^{bcc} c_2^\alpha c_4^\alpha \quad (10)$$

$$\mu_4^\alpha(T, P, c_i^\alpha) =^0 G_{Si}^{bcc} + RT \log(c_4^\alpha) - L_{Fe,Mn}^{bcc} c_1^\alpha c_2^\alpha - L_{Fe,Ni}^{bcc} c_1^\alpha c_3^\alpha + L_{Fe,Si}^{bcc} c_1^\alpha (c_1^\alpha + c_2^\alpha + c_3^\alpha) - L_{Mn,Ni}^{bcc} c_2^\alpha c_3^\alpha + L_{Mn,Si}^{bcc} c_2^\alpha (c_1^\alpha + c_2^\alpha + c_3^\alpha) \quad (11)$$

The driving force for the diffusion of the substitutional alloy is given by the diffusion potential [14]. We assumed that the substitution of Fe atoms for Mn, Ni, and Si atoms was dominant. Therefore,

$$\lambda_{1 \rightarrow 2}^\alpha = \frac{\partial G^\alpha(c_i^\alpha, t)}{\partial c_2^\alpha} = \mu_2^\alpha(T, P, c_i^\alpha) - \mu_1^\alpha(T, P, c_i^\alpha) \quad (12)$$

To confirm the relation in Eq. 12, we introduced the case of the ideal binary solution. We assumed that the system is an A-B binary system.

$$G(c_A, c_B, t) =^0 G_{ACA} +^0 G_{BCB} + RT[c_A \log(c_A) + c_B \log(c_B)] \quad (13)$$

where $c_A + c_B = 1.0$.

$$\lambda_{B \rightarrow A} = \frac{\partial G(c_A, c_B, t)}{\partial c_A} =^0 G_A -^0 G_B + RT \log(c_A/c_B) \quad (14)$$

The chemical potentials of the A and B species are given as follows:[14],

$$\mu_A =^0 G_A + RT \log(c_A) \quad (15)$$

$$\mu_B =^0 G_B + RT \log(c_B) \quad (16)$$

Therefore, from Eqs. 14, 15, and 16, we showed that the relation 17 is correct.

$$\lambda_{B \rightarrow A} = \mu_A - \mu_B \quad (17)$$

In Kim's model [9], the diffusion potentials of all phases are assumed to be equal under equilibrium. For a stoichiometric compound, the diffusion potential of each element cannot be defined. Therefore, we do not apply the equal diffusion potential condition in the case of the T3 and T7 precipitates. The T6 precipitate has the Ni and Si solubility range, so we apply the equal diffusion potential condition.

2. Iterative solver for composition field

We solved the Cahn- Hilliard equation (Eq. 18) to relax the composition field of each component.

$$\frac{\partial c_i(\mathbf{r}, t)}{\partial t} = \nabla M_i \nabla \left(\frac{\delta G}{\delta c_i(\mathbf{r}, t)} \right) \quad (i = 2, 3, 4) \quad (18)$$

$$\frac{\partial \phi^\theta(\mathbf{r}, t)}{\partial t} = -L^\theta \frac{\delta G}{\delta \phi^\theta(\mathbf{r}, t)} \quad (\theta = T3, T6, T7) \quad (19)$$

where

$$g(\phi^\theta) = \frac{H^\theta}{2} (\phi^\theta)^2 (\phi^\theta - 1)^2 + (\phi^\theta)^2 \sum_{\psi \neq \theta} (\phi^\psi)^2 \quad (20)$$

To determine M_i in Eq. 18, we adopted the relation in ref. [7, 8].

$$D_i(\phi^\theta, T) = (1 - \phi^\theta) D_i^\alpha(T) + \phi^\theta D_i^\beta(T) \quad (21)$$

We used the relation $D_i^\theta(T) = D_i^\theta \exp(-Q_i^\theta/RT)$ to determine the diffusivity; the parameters used to determine the value are listed in Table I.

Elements	Phase	$^0 D_i^\theta$ (m^2/s)	Q_i^θ (J/mol)
Mn	α (bcc)	1.5×10^{-4}	2.34×10^5
Mn	γ (fcc)	1.6×10^{-5}	2.62×10^5
Ni	α (bcc)	4.2×10^{-3}	2.68×10^5
Ni	γ (fcc)	7.7×10^{-5}	2.81×10^5
Si	α (bcc)	1.7×10^{-4}	2.29×10^5
Si	γ (fcc)	1.59×10^{-5}	2.56×10^5

TABLE I. The values of the diffusivity and activation element of each element. All values except the data for Si in fcc Fe are taken from ref. [15]. Diffusivity and activation data of Si in fcc were not found in the references, so we used unpublished experimental results.

Eq. 18 can be rewritten as follows by using the extended Kim's model when α and T6 phases are under equilibrium [9, 16].

$$\frac{\partial c_i(\mathbf{r}, t)}{\partial t} = \nabla \cdot \left(\frac{D_i(\phi^{T6}, T)}{G_{c_i c_i}} (G_{c_i \phi^{T6}} \nabla \phi^{T6} + G_{c_i c_i} \nabla c_i) \right) \quad (i = 2, 3, 4) \quad (22)$$

$$G_{c_i c_i}(c_i, \phi^{T6}) = \frac{G_{c_i c_i}^\alpha(c_i) G_{c_i c_i}^{T6}(c_i)}{[1 - h(\phi^{T6})] G_{c_i c_i}^{T6}(c_i) + h(\phi^{T6}) G_{c_i c_i}^\alpha(c_i)} \quad (23)$$

where,

$$G_{c_i c_i}^\alpha(c_i) = \frac{\partial^2 G^\alpha}{\partial (c_i^\alpha)^2} \quad (24)$$

$$G_{c_i c_i}^{T6}(c_i) = \frac{\partial^2 G^{T6}}{\partial (c_i^{T6})^2} \quad (25)$$

$$\frac{G_{c_i \phi^{T6}}(c_i, \phi^{T6})}{G_{c_i c_i}(c_i, \phi^{T6})} = h'(\phi^{T6})(c_i^\alpha - c_i^{T6}) \quad (26)$$

Therefore, we have the conclusion in ref. [9] ($i = 2, 3, 4$).

$$\frac{\partial c_i(\mathbf{r}, t)}{\partial t} = \nabla (D_i(\phi^{T6}) \nabla c_i) + \nabla (D_i(\phi^{T6}) h'(\phi^{T6})(c_i^\alpha - c_i^{T6}) \nabla \phi^{T6}) \quad (27)$$

Finally, we obtain the modified form of Eq. 19 as follows:

$$\frac{\partial \phi^{T6}(\mathbf{r}, t)}{\partial t} = L^{T6} \left(\kappa^{T6} \nabla \phi^{T6} + h'(\phi^{T6}) [G^\alpha(c_i^\alpha) - G^{T6}(c_i^{T6}) - \sum_{i=2}^4 ((c_i^\alpha - c_i^{T6}) G_{c_i})] - g'(\phi^{T6}) \right) \quad (28)$$

Since all concentrations are fixed for the T3 and T7 precipitates, we can directly calculate c_i^α when the T3 and T7 phases are present in the system by using the relation Eq. 30. (c_i^θ is constant.)

$$c_i(\mathbf{r}, t) = c_i^\theta h(\phi^\theta) + c_i^\alpha(\mathbf{r}, t) [1 - h(\phi^\theta)] \quad (\theta = T3, T7) \quad (29)$$

$$c_i^\alpha(\mathbf{r}, t) = \frac{c_i(\mathbf{r}, t) - c_i^\theta h(\phi^\theta)}{1 - h(\phi^\theta)} \quad (\theta = T3, T7) \quad (30)$$

For the T6 phase, $c_3^{T6}(\mathbf{r}, t)$ and $c_4^{T6}(\mathbf{r}, t)$ are not constant, so we calculated $y_3^{II}(\mathbf{r}, t)$ and $y_4^{II}(\mathbf{r}, t)$. The procedure to determine the terms $y_3^{II}(\mathbf{r}, t)$ and $y_4^{II}(\mathbf{r}, t)$ in Eq. 6 is described below:

1. Obtain $c_i(\mathbf{r}, t)$ by solving Eq. 27.
2. Obtain $\phi^{T6}(\mathbf{r}, t)$ by solving Eq. 28.
3. Assume $c_3^{T6, temp}(\mathbf{r}, t)$ and $c_3^{\alpha, temp}(\mathbf{r}, t)$. For the first iteration, $c_3^{T6, temp}(\mathbf{r}, t)$ and $c_3^{\alpha, temp}(\mathbf{r}, t)$ set the values of the former time step. When the number of the iterations is equal to or larger than 2, the values are set at step 6.
4. Check whether the relation $c_3^{temp}(\mathbf{r}, t) = c_3^{T6, t}(\mathbf{r}, t) h(\phi^{T6}) + c_3^{\alpha, t}(\mathbf{r}, t) [1 - h(\phi^{T6})]$ is satisfied. Assume $c_3^{T6, temp}(\mathbf{r}, t)$ and $c_3^{\alpha, temp}(\mathbf{r}, t)$, satisfying $\frac{\partial G^{T6}}{\partial c_3^{T6, temp}} = \frac{\partial G^\alpha}{\partial c_3^{\alpha, temp}}$. (common tangent)
5. If the relation in step 4 is satisfied, $c_3^{T6}(\mathbf{r}, t) = c_3^{T6, temp}(\mathbf{r}, t)$ and $c_3^\alpha(\mathbf{r}, t) = c_3^{\alpha, temp}(\mathbf{r}, t)$.
 - (a) Determine $c_4^{T6}(\mathbf{r}, t)$ using the relation Eq. 35.

Since,

$$c_4^{T6} = \frac{2}{3} - c_3^{T6} \quad (31)$$

From the relation,

$$\frac{\partial G^{T6}}{\partial c_3^{T6}} = \frac{\partial G^{T6}}{\partial c_4^{T6}} \frac{\partial c_4^{T6}}{\partial c_3^{T6}} = -\frac{\partial G^{T6}}{\partial c_4^{T6}} \quad (32)$$

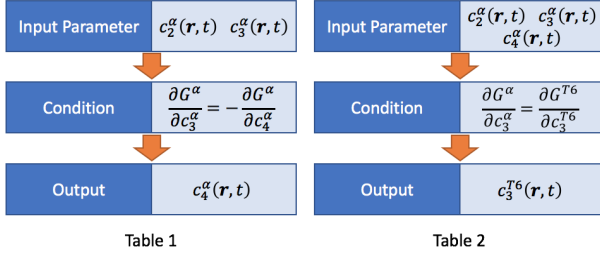


Fig. 1. Inputs, conditions, and outputs of two tables

The Eqs. 33 and 34 represent the common tangent condition:

$$\frac{\partial G^{T6}}{\partial c_3^{T6}} = \frac{\partial G^\alpha}{\partial c_3^\alpha} \quad (33)$$

$$\frac{\partial G^{T6}}{\partial c_4^{T6}} = \frac{\partial G^\alpha}{\partial c_4^\alpha} \quad (34)$$

Therefore, from Eqs. 32 to 34,

$$\frac{\partial G^\alpha}{\partial c_3^\alpha} = -\frac{\partial G^\alpha}{\partial c_4^\alpha} \quad (35)$$

(b) Calculate $y_3^H(\mathbf{r}, t)$ and $y_4^H(\mathbf{r}, t)$ from the relation $y_3^H = \frac{3}{2}c_3^{T6}$ and $y_4^H = \frac{3}{2}c_4^{T6}$.

(c) Procedure complete.

6. If the relation in step 4 is not satisfied, modify $c_3^{T6,t}(\mathbf{r}, t)$ (step value is 3.0×10^{-7}) appropriately and find $c_3^{\alpha,temp}(\mathbf{r}, t)$, which satisfies $\frac{\partial G^{T6}}{\partial c_3^{T6,temp}} = \frac{\partial G^\alpha}{\partial c_3^{\alpha,temp}}$. Go to step 3.

For the numerical efficiency, we assumed that $\frac{\partial G^{T6}}{\partial c_3^{T6,temp}} = \frac{\partial G^\alpha}{\partial c_3^{\alpha,t}}$, when $\left| \frac{\partial G^{T6}}{\partial c_3^{T6,temp}} - \frac{\partial G^\alpha}{\partial c_3^{\alpha,temp}} \right| < 1.0^{-8}$ in step 4. We applied the same assumption for the equal sign in steps 5 and 6.

We constructed two sets of tables (pre-calculated values) of the compositions as described in Fig. 1 to reduce the computation time. The inputs of Table 1 are c_2^α and c_3^α , and we obtain c_4^α using Eq. 35. Then, we obtain c_4^{T6} by inputting c_2^α , c_3^α , and c_4^α into Eq. 33. Once we determine c_3^{T6} , we can easily calculate c_4^{T6} using the relation $c_3^{T6} = \frac{2}{3} - c_4^{T6}$. To apply the condition of Tables 1 and 2, we used the Newton-Raphson method to obtain the outputs.

IV. COMPUTATIONAL DETAILS AND PARAMETER NORMALIZATION

We adopted the forward Euler scheme to discretize Eqs. 36 and 37 [17].

Eqs. 18 and 19 are restated as Eqs. 36 and 37,

$$\frac{\partial c_i^\alpha(\mathbf{r}, t)}{\partial t} = \nabla M_i \nabla (\lambda_{1 \rightarrow i}^\alpha - \kappa_i \nabla^2 c_i^\alpha(\mathbf{r}, t)) (i = 2, 3, 4) \quad (36)$$

$$\frac{\partial \phi^\theta(\mathbf{r}, t)}{\partial t} = -L^\theta \left(\frac{\partial G}{\partial \phi^\theta(\mathbf{r}, t)} - \omega^\theta \nabla^2 \phi^\theta(\mathbf{r}, t) \right) (\theta = T3, T6, T7) \quad (37)$$

where

$$\begin{aligned} \lambda_{1 \rightarrow 2}^\alpha = & {}^0 G_{Mn}^{bcc} - {}^0 G_{Fe}^{bcc} + RT[\log(c_2^\alpha) - \log(c_1^\alpha)] + L_{Fe,Mn}^{bcc} \\ & (c_1^\alpha - c_2^\alpha) - L_{Fe, Ni}^{bcc} c_3^\alpha - L_{Fe, Ni}^{bcc} c_1^\alpha c_3^\alpha - L_{Fe, Si}^{bcc} c_4^\alpha + L_{Mn, Ni}^{bcc} c_2^\alpha \\ & - ({}^1 L_{Fe, Si}^{bcc} + 2^2 L_{Fe, Si}^{bcc} (c_1^\alpha - c_4^\alpha)) c_1^\alpha c_4^\alpha + L_{Mn, Si}^{bcc} c_4^\alpha \\ & + {}^1 L_{Mn, Si}^{bcc} c_2^\alpha c_4^\alpha \end{aligned} \quad (38)$$

$$\begin{aligned} \lambda_{1 \rightarrow 3}^\alpha = & {}^0 G_{Ni}^{bcc} - {}^0 G_{Fe}^{bcc} + RT[\log(c_3^\alpha) - \log(c_1^\alpha)] - L_{Fe, Mn}^{bcc} \\ & c_2^\alpha + L_{Fe, Ni}^{bcc} (c_1^\alpha - c_3^\alpha) - ({}^1 L_{Fe, Si}^{bcc} + 2^2 L_{Fe, Si}^{bcc} (c_1^\alpha - c_4^\alpha)) \\ & c_1^\alpha c_4^\alpha + L_{Mn, Ni}^{bcc} c_2^\alpha - 2^1 L_{Fe, Ni}^{bcc} c_1^\alpha c_3^\alpha - L_{Fe, Si}^{bcc} c_4^\alpha \end{aligned} \quad (39)$$

$$\begin{aligned} \lambda_{1 \rightarrow 4}^\alpha = & {}^0 G_{Si}^{bcc} - {}^0 G_{Fe}^{bcc} + RT[\log(c_4^\alpha) - \log(c_1^\alpha)] \\ & - L_{Fe, Mn}^{bcc} c_2^\alpha - L_{Fe, Ni}^{bcc} c_3^\alpha + L_{Fe, Si}^{bcc} (c_1^\alpha - c_4^\alpha) - 2({}^1 L_{Fe, Si}^{bcc} \\ & + 2^2 L_{Fe, Si}^{bcc} (c_1^\alpha - c_4^\alpha)) c_1^\alpha c_4^\alpha - {}^1 L_{Fe, Ni}^{bcc} c_1^\alpha c_3^\alpha + L_{Mn, Si}^{bcc} c_4^\alpha \\ & - {}^1 L_{Mn, Si}^{bcc} c_2^\alpha c_4^\alpha \end{aligned} \quad (40)$$

In our simulations, we used the energy normalized by RT where $R = 8.3144598 \text{ J/mol} \cdot \text{K}$ and the temperature $T = 550 \text{ K}$. The diffusivity values were normalized by $D_2^\alpha(T)$. The non-dimensional time step $\Delta t = 1.0 \times 10^{-6}$ when the $T3$ precipitate existed, and $\Delta t = 1.0 \times 10^{-6}$ when the $T6$ or $T7$ precipitate existed. $\Delta x = \Delta y$ was set to 1.0. κ_i in Eq. 37 was set to 1.0 and $\omega^\theta = 2.0$ and $L^\theta = 0.01$ in Eq. 37.

We performed 2D simulations, and the system size was $64\Delta x \times 64\Delta y$. The initial precipitate radius was $15.0\Delta x$. Initially, we put $\phi^\theta = 1.0$ inside the particle with the sharp interface (Outside $\phi^\theta = 0$). To make the particle/matrix interface diffused, we solved Eq. 19 with the assumption of $G = \frac{1}{2}(\phi^\theta)^2(\phi^\theta - 1)^2$. (100 iterations). After we obtained ϕ^θ with the diffused interface, we put the concentration profile as follows:

For the matrix, the initial compositions at α phase were $c_2^\alpha = 0.008$, $c_3^\alpha = 0.008$, $c_4^\alpha = 0.00808$. For the $T6$ precipitate, $c_3^{T6} = 0.459234067$ and $c_4^{T6} = 0.2074326$, when Eqs. 33 and 35 are satisfied. For the $T3$ and $T7$ cases, the compositions of the precipitates were fixed and the initial compositions of the α phase were assumed to be equal to the values of the $T6$ case. Then, we put the initial composition using the Eq. 1.

V. RESULTS

In Fig. 2, the $T6$ precipitate maintained their initial state during the simulation. This means that, the $T6$ precipitate is thermodynamically stable. Since the $T3$ and $T7$ phases are unstable, these precipitates shrink with time, and the $T7$ precipitate radius decreases more rapidly than that of the $T3$

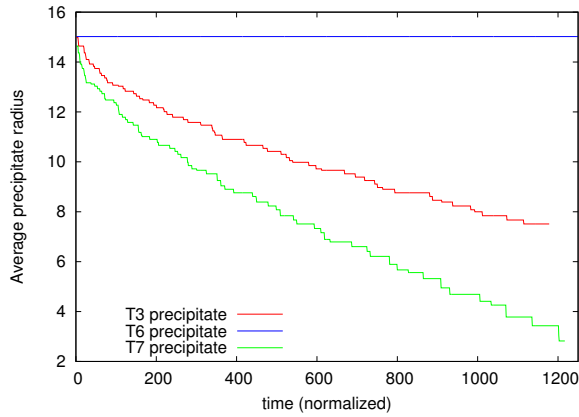


Fig. 2. Precipitate radius of T3, T6, and T7 precipitates

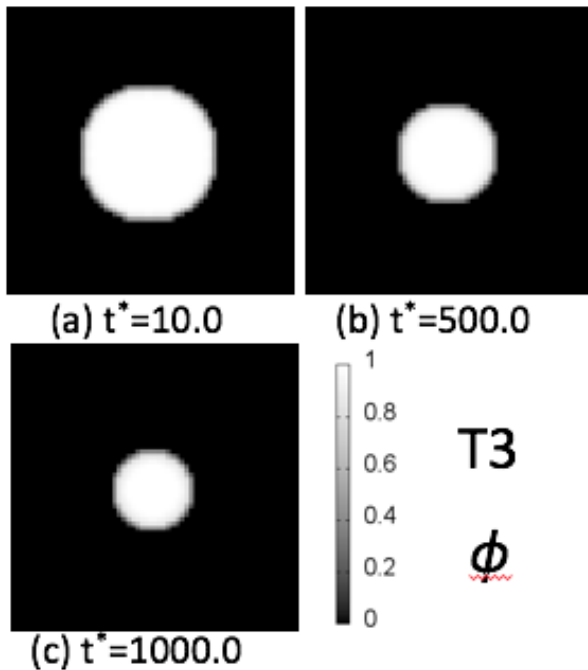


Fig. 3. Distribution of ϕ^{T3} when $t^* = 10.0$, $t^* = 500.0$, and $t^* = 1000.0$

. ϕ^{T3} value is 1.0 inside the particle and 0.0 in the matrix.

precipitate does. We performed CALPHAD modeling using ThermoCalc Software with the implementation of UW1 database [3] with $c_2^\alpha = 0.008$, $c_3^\alpha = 0.008$, $c_4^\alpha = 0.00808$, and $T = 550K$. The equilibrium phases were BCC(A2) (98.940 mol%) and T6 (1.363 mol%). Also, T6 phase is quite dominantly observed in neutron-irradiated RPV steel [3, 4, 5]. Therefore, we concluded that our simulation result is consistent with the results obtained from the CALPHAD modeling and former experimental studies.

As shown in Fig. 3, the T3 precipitate shrinks with time.

In Figs. 4 to 6, we observed a wide diffused concentration profile zone (DCPZ) between the precipitate and matrix. In particular, the DCPZ in Fig. 5 is the widest (Ni concentration). When $T = 550K$, $D_2^\alpha(T) = 8.976 \times 10^{-27} m^2/s$, $D_3^\alpha(T) =$

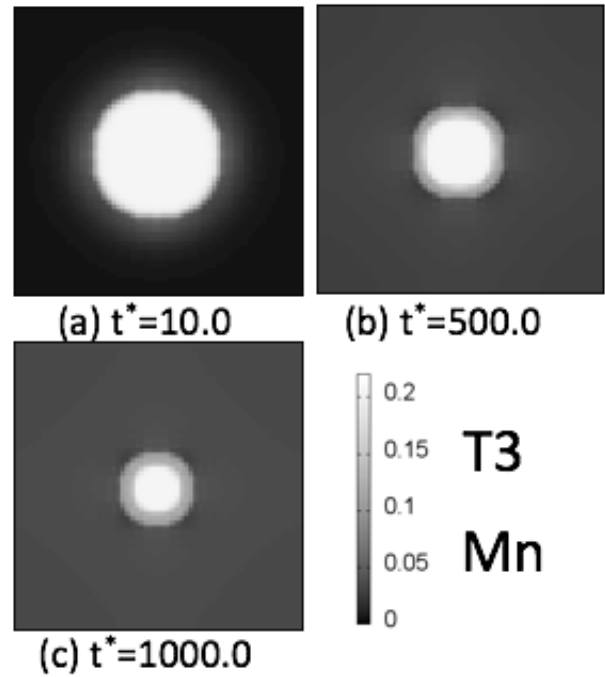


Fig. 4. Distribution of c_2^{T3} (Mn) when $t^* = 10.0$, $t^* = 500.0$, and $t^* = 1000.0$

. The maximum c_2^{T3} value is 0.22.

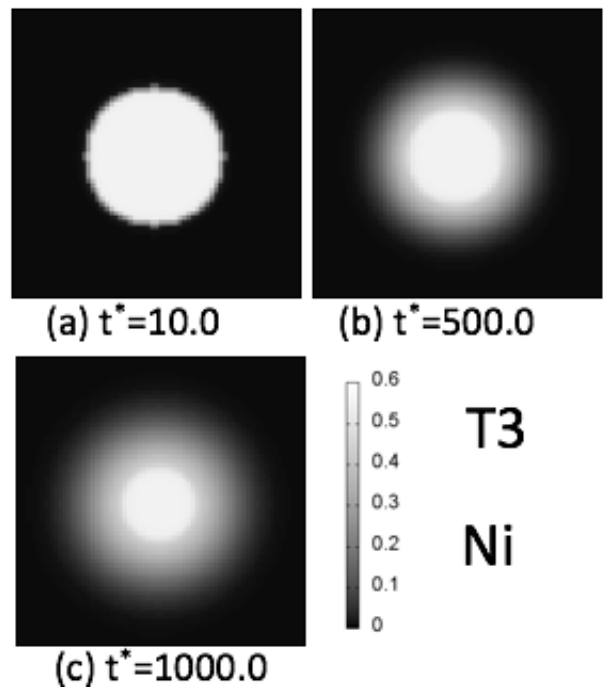


Fig. 5. Distribution of c_3^{T3} (Ni) when $t^* = 10.0$, $t^* = 500.0$, and $t^* = 1000.0$

. The maximum c_3^{T3} value is 0.6.

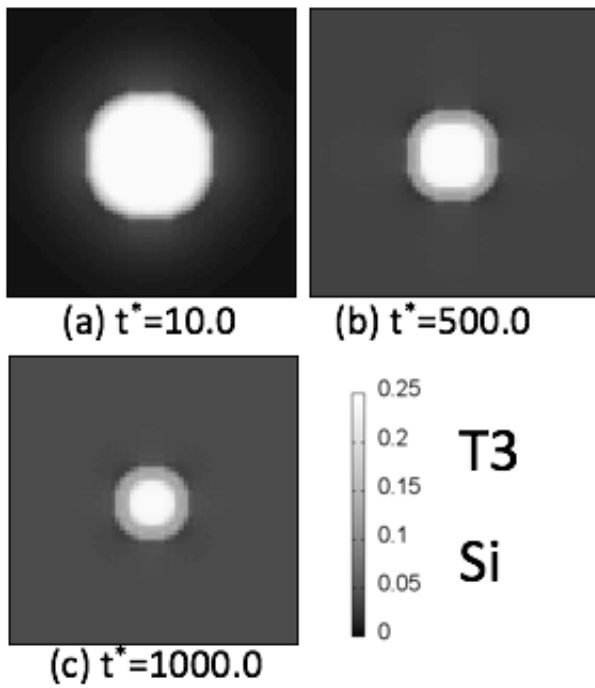


Fig. 6. Distribution of c_4^{T3} (Si) when $t^* = 10.0$, $t^* = 500.0$, and $t^* = 1000.0$

. The maximum c_4^{T3} value is 0.25.

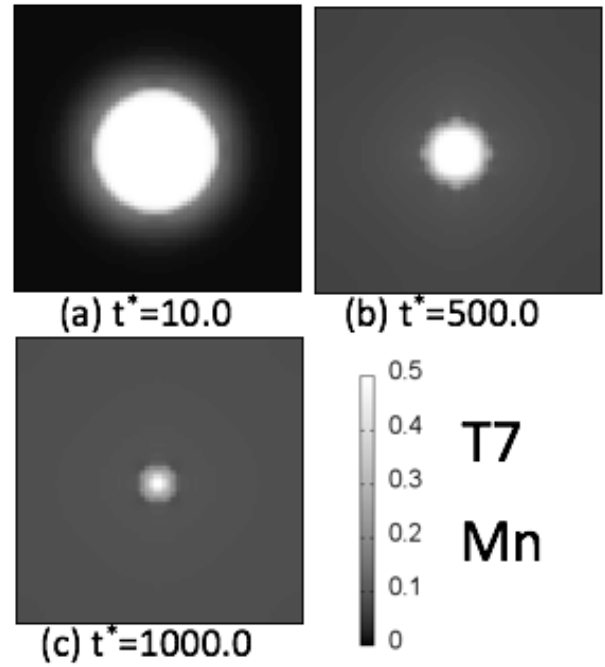


Fig. 8. Distribution of c_2^{T7} (Mn) when $t^* = 10.0$, $t^* = 500.0$, and $t^* = 1000.0$

. The maximum c_2^{T7} value is 0.5.

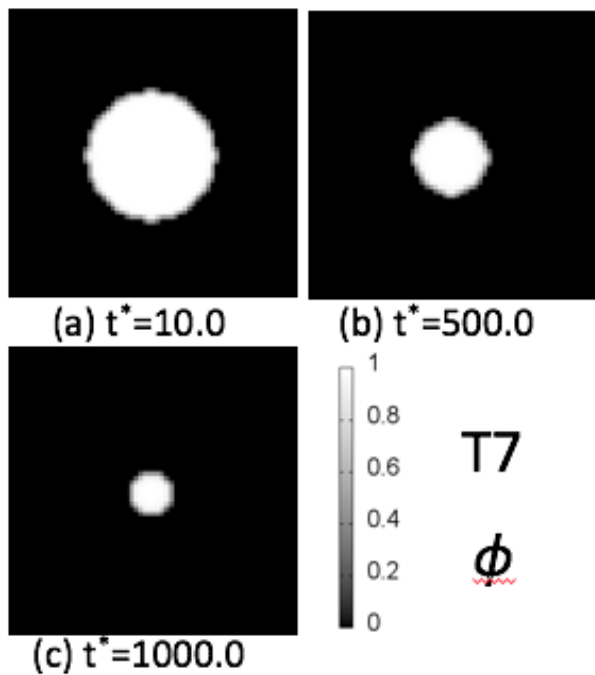


Fig. 7. Distribution of ϕ^{T7} when $t^* = 10.0$, $t^* = 500.0$, and $t^* = 1000.0$

. ϕ^{T7} value is 1.0 inside the particle and 0.0 in the matrix.

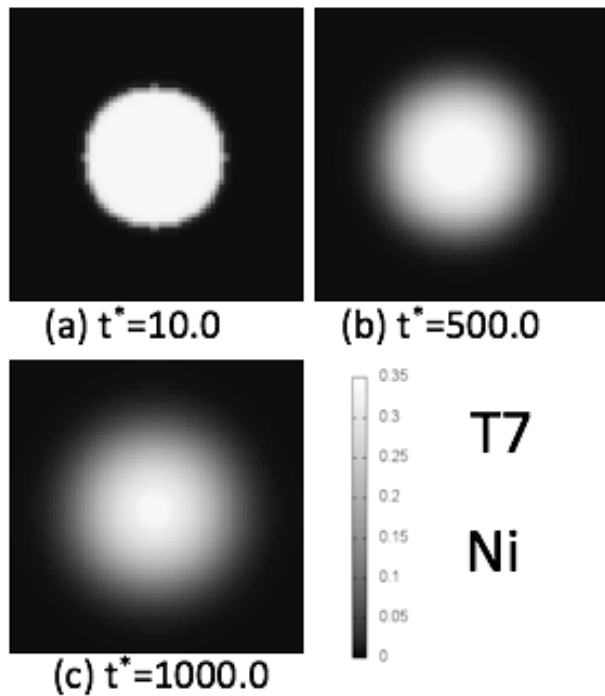


Fig. 9. Distribution of c_3^{T7} (Ni) when $t^* = 10.0$, $t^* = 500.0$, and $t^* = 1000.0$

. The maximum c_3^{T7} value is 0.35.

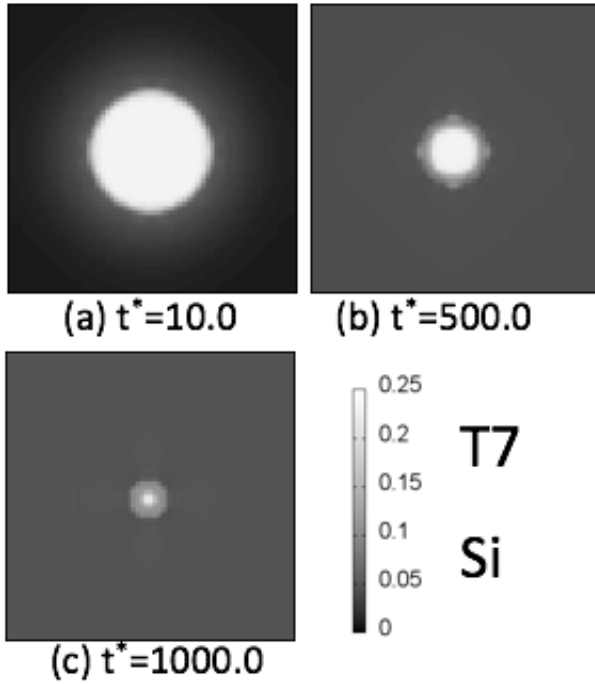


Fig. 10. Distribution of c_4^{T7} (Si) when $t^* = 10.0$, $t^* = 500.0$, and $t^* = 1000.0$

. The maximum c_4^{T7} value is 0.25.

$1.483 \times 10^{-28} m^2/s$, and $D_4^\alpha(T) = 3.036 \times 10^{-26} m^2/s$. Since $D_3^\alpha(T)$ is far smaller than even $D_2^\alpha(T)$, the DCPZ is thicker in Fig. 5 than that in Figs. 4 and 6. For the T7 precipitate, we also observed DCPZ in Figs. 8 to 10, and the widest DCPZ is found in Fig. 9 (Ni concentration).

VI. DISCUSSION AND FUTURE WORKS

According to the classical nucleation theory [14], the critical spherical nucleus radius, when $\alpha \rightarrow \beta$ phase transformation occurs, is given by:

$$r^* = \frac{2\gamma}{(\Delta G_\alpha - \Delta G_\beta)} \quad (41)$$

where γ is the isotropic interfacial energy and $\Delta G_\alpha - \Delta G_\beta$ is the bulk energy difference between the α and β phases. The stability of the precipitate can be evaluated in terms of the bulk energy difference using the CALPHAD method. On the other hand, in the phase-field method, the phase stability is examined with the consideration of not only the bulk energy difference but also the interfacial energy. So far, we do not have reliable information about the interfacial energy and width between α and the precipitated phase. Therefore, we assumed that ω^θ when ($\theta = T3, T6, T7$) in Eq. 37 is 2.0. In reality, the misfit strain exists at a coherent or semi-coherent interface [14]. Therefore, the elastic effect needs to be considered to estimate the particle stability more accurately. The critical radius of the nucleus is generally larger than the value obtained using Eq. 41.

$$r^* = \frac{2(\gamma + E_{es})}{(\Delta G_\alpha - \Delta G_\beta)} \quad (42)$$

where E_{es} represents the elastic energy per unit area between precipitate particles and the matrix. Also, the elastic effect can induce a deviation in the precipitate particle morphology from the spherical shape [12, 18, 19]. When a particle is not spherical, analytical determination of the critical nucleus size becomes more complicated. Therefore, a numerical modeling method, such as the phase-field simulation, is a powerful approach to estimate the precipitate stability. Due to lack of information regarding the interface structure between the matrix and a precipitate particle, we do not consider the elastic effect in this study. However, in future, we aim to study the particle/matrix interface structure, and thereafter, we plan to perform the precipitate-evolution modeling with the incorporation of the elastic effect.

For the unstable precipitates, such as the T3 and T7 precipitates in Fig. 2, the shrinking rate is an important factor. In our simulation, the T7 precipitate disappeared at a faster rate than the T3 precipitate. The dissolution rate in the case of an incoherent interface is determined by three factors:

1. Chemical driving force. (bulk energy difference)
2. Interface energy between the matrix and precipitate
3. Solute mobility

Within the CALPHAD framework, the precipitate stability can be predicted using only factor 1. In the phase-field modeling, we quantitatively consider factors 1 and 3. So far, we have assumed that the parameter determining interfacial energy is constant for all precipitated phases. As explained above, we aim to analyze the interface between the bcc matrix and precipitates in the future, and thereafter, we will consider factor 2 in determining the precipitate stability.

VII. ACKNOWLEDGMENTS

This study was supported by a National Research Foundation of Korea (NRF) grant funded by the Korean government (MSIP) (No. 2012M2A8A4025886).

REFERENCES

1. G. ODETTE and G. LUCAS, "Embrittlement of nuclear reactor pressure vessels," *JOM*, **53**, 7, 18–22 (2001).
2. G. ODETTE and G. LUCAS, "Recent progress in understanding reactor pressure vessel steel embrittlement," *Radiation effects and defects in solids*, **144**, 1-4, 189–231 (1998).
3. W. XIONG, H. KE, R. KRISHNAMURTHY, P. WELLS, L. BARNARD, G. R. ODETTE, and D. MORGAN, "Thermodynamic models of low-temperature Mn–Ni–Si precipitation in reactor pressure vessel steels," *MRS Communications*, **4**, 03, 101–105 (2014).
4. D. SPROUSTER, J. SINSHEIMER, E. DOORYHEE, S. GHOSE, P. WELLS, T. STAN, N. ALMIRALL, G. ODETTE, and L. ECKER, "Structural characterization of nanoscale intermetallic precipitates in highly neutron irradiated reactor pressure vessel steels," *Scripta Materialia*, **113**, 18–22 (2016).
5. P. B. WELLS, T. YAMAMOTO, B. MILLER, T. MILOT, J. COLE, Y. WU, and G. R. ODETTE, "Evolution of manganese–nickel–silicon-dominated phases in highly

- irradiated reactor pressure vessel steels,” *Acta Materialia*, **80**, 205–219 (2014).
6. T. KOYAMA and H. ONODERA, “Computer simulation of phase decomposition in Fe-Cu-Mn-Ni quaternary alloy based on the phase-field method,” *Materials transactions*, **46**, 6, 1187–1192 (2005).
 7. T. KOYAMA, K. HASHIMOTO, and H. ONODERA, “Phase-field simulation of phase transformation in Fe-Cu-Mn-Ni quaternary alloy,” *Materials transactions*, **47**, 11, 2765–2772 (2006).
 8. S. BINER, W. RAO, and Y. ZHANG, “The stability of preprecipitates and the role of lattice defects in Fe-1at% Cu-1at% Ni-1at% Mn alloy: A phase-field model study,” *Journal of Nuclear Materials*, **468**, 9–16 (2016).
 9. S. G. KIM, W. T. KIM, and T. SUZUKI, “Phase-field model for binary alloys,” *Physical review e*, **60**, 6, 7186 (1999).
 10. J. W. CAHN and J. E. HILLIARD, “Free energy of a nonuniform system. I. Interfacial free energy,” *The Journal of chemical physics*, **28**, 2, 258–267 (1958).
 11. S. M. ALLEN and J. W. CAHN, “A microscopic theory for antiphase boundary motion and its application to antiphase domain coarsening,” *Acta Metallurgica*, **27**, 6, 1085–1095 (1979).
 12. J. ZHU, T. WANG, A. ARDELL, S. ZHOU, Z. LIU, and L. CHEN, “Three-dimensional phase-field simulations of coarsening kinetics of γ particles in binary Ni–Al alloys,” *Acta Materialia*, **52**, 9, 2837–2845 (2004).
 13. A. DINSDALE, “SGTE data for pure elements,” *Calphad*, **15**, 4, 317–425 (1991).
 14. D. A. PORTER, K. E. EASTERLING, and M. SHERIF, *Phase Transformations in Metals and Alloys, (Revised Reprint)*, CRC press (2009).
 15. *Metals Data book 3rd ed.*, Japan Institute of Metals, Maruzen, Tokyo (2004).
 16. S. HU, J. MURRAY, H. WEILAND, Z. LIU, and L. CHEN, “Thermodynamic description and growth kinetics of stoichiometric precipitates in the phase-field approach,” *Calphad*, **31**, 2, 303–312 (2007).
 17. L.-Q. CHEN and W. YANG, “Computer simulation of the domain dynamics of a quenched system with a large number of nonconserved order parameters: The grain-growth kinetics,” *Physical Review B*, **50**, 21, 15752 (1994).
 18. A. ARDELL and R. NICHOLSON, “The coarsening of γ ’ in Ni–Al alloys,” *Journal of Physics and Chemistry of Solids*, **27**, 11, 1793–1794 (1966).
 19. J. RIBIS and Y. DE CARLAN, “Interfacial strained structure and orientation relationships of the nanosized oxide particles deduced from elasticity-driven morphology in oxide dispersion strengthened materials,” *Acta materialia*, **60**, 1, 238–252 (2012).